Thermodynamic behavior of CrF$_2$ corrosion product in the molten LiF-ThF$_4$ salt system

Dumaire, T.; Walter, O.; Beneš, O.; Griveau, J. C.; Colineau, E.; Konings, R. J.M.; Smith, A. L.

Important note
To cite this publication, please use the final published version (if applicable).
Please check the document version above.

Thermodynamic behavior of CrF$_2$ corrosion product in the molten LiF-ThF$_4$ salt system

T. Dumaire [a,b], O. Walter [b], O. Beneš [b], J.-C. Griveau [b], E. Colineau [b], R.J.M. Konings [a,b], A.L. Smith [a,*]

[a] *Delft University of Technology, Faculty of Applied Sciences, Radiation Science & Technology Department, Mekelweg 15, 2629 JB Delft, The Netherlands*
[b] *European Commission, Joint Research Centre (JRC), Karlsruhe, Germany*

A B S T R A C T

This work examines the thermochemistry of the chromium difluoride CrF$_2$ corrosion product in the molten LiF $-$ ThF$_4$ fuel salt system. Through a combination of experimental investigations and thermodynamic modeling assessment, the study elucidates the thermodynamic properties, phase diagram equilibria, and overall thermodynamic behavior of CrF$_2$ corrosion product, following dissolution from a structural material to the molten salt fuel environment. In this work, two different synthesis methods were developed for pure CrF$_2$, further allowing to experimentally measure the phase equilibria in the LiF $-$ CrF$_2$, CrF$_2$ $-$ ThF$_4$, and LiF $-$ CrF$_2$ $-$ ThF$_4$ systems. Then, thermodynamic models were developed using the CALPHAD method based on the quasichemical model in the quadruplet approximation.

1. Introduction

To cope with climate change and limit global warming to below 1.5 °C, the recommendations of the Intergovernmental Panel on Climate Change require a profound adaptation of the energy production mix [1]. A wider use of nuclear power is suggested as one of the solutions to replace fossil fuels with high expectations for advanced reactor technologies.

The Molten Salt Reactor (MSR) is an advanced reactor design of the 4th generation, that uses liquid fluoride or chloride salts as both the fuel and coolant [2–5]. MSRs offer several advantages compared to traditional solid fueled and water-cooled nuclear reactors, such as inherent safety, with built-in passive safety mechanisms. MSRs can also accommodate a wide variety of fertile and fissile materials, including thorium, natural or depleted uranium, or re-processed plutonium, which are abundant naturally or from the nuclear fuel cycle of traditional Light Water Reactors [6].

The LiF $-$ ThF$_4$ $-$ UF$_4$ salt mixture is one of the reference fuel salt selected for the Molten Salt Fast Reactor (MSFR) concept [5]. Lithium fluoride (LiF) serves as the solvent, or matrix, for the other components in the fuel mixture. It has good heat transfer properties, is chemically stable at high temperatures [7], and is compatible with a fast neutron spectrum as long as it is enriched in lithium-7 (^{7}Li) [8]. Thorium tetrafluoride (ThF$_4$), with the isotope ^{232}Th, is a fertile material, meaning it can capture neutrons and be converted into fissile uranium-233

(^{233}U) [9,10]. Uranium tetrafluoride (UF$_4$) is a fissile material, which can sustain a nuclear chain reaction under its enriched forms in isotopes ^{233}U and ^{235}U.

Fluoride salts are corrosive in their molten state at high temperatures, which implies high requirements on the materials composing the reactor vessel [11]. Ni-based alloys with a high concentration of chromium, such as Hastelloy-N (7 wt% chromium content), were recommended in the preliminary studies realized by the Oak Ridge National Laboratory (ORNL) in the 1960s and 1970s during the Molten Salt Reactor Experiment (MSRE) and Molten Salt Breeder Reactor (MSBR) program [12]. Experimental investigations were realized in thermal convection loops, with the aim to simulate the material degradation of key components of the reactor (e.g. hot and cold parts, welded connections, angles). Hastelloy-N specimens were exposed, during nine years, to a LiF $-$ BeF$_2$ $-$ ZrF$_4$ $-$ UF$_4$ $-$ ThF$_4$ (approximately 70-23-5-1–1 mol%) fuel salt, circulating between 833 K (560 °C) and 973 K (700 °C) [13]. The different cross section observations, by macro and microstructural analyses, showed the formation of interstitial voids due to chromium depletion (and to some extent iron depletion). The post-analysis of the salt composition after nine years showed a significant increase in the concentration of Cr in the fuel salt (from 100 ppm to 1800 ppm) [13,14]. These observations were confirmed by several subsequent studies [15–18]. According to the different investigations mentioned, the presence of oxidized chromium in the salt solution is

Table 1

Supplier and purity of the chemicals used in this work.

Compound	Supplier	Purity	Concentration
LiF powder	Alfa Aesar	99.99%	
CrF$_3$ powder	Alfa Aesar	99.98% (metal basis)	
Chromium powder (1250 mesh)	Alfa Aesar	99.8% (metal basis)	
Acetic acid	Alfa Aesar	99.7%	
Acetic anhydride	Alfa Aesar	99+%	
Hydrobromic acid	Alfa Aesar		47%
Ammonium hydroxide	Alfa Aesar		25%
Hydrofluoric acid	Bernd Kraft		47 to 51%

mainly driven by the redox equilibrium:

$$2\,UF_4 + Cr^0 \rightleftharpoons 2\,UF_3 + CrF_2$$
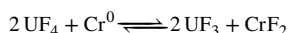
To some extent, ionic impurities Ni^{2+} and Fe^{2+} dissolved into the salt after corrosion can also contribute to the further depletion of chromium from the structural material [13,14], according to the following equilibria:

$$NiF_2 + Cr \rightleftharpoons Ni + CrF_2$$
$$FeF_2 + Cr \rightleftharpoons Fe + CrF_2$$
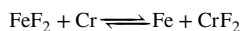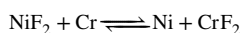
It was also found that oxidized chromium, in the cationic form of Cr^{2+} or Cr^{3+}, could enhance the kinetics of redox reactions involved in the degradation of structural materials in contact with Li-based molten fluoride salts [19]. Based on their first results, ORNL researchers initially considered CrF$_3$ to be more stable, but the studies were focused on dissolution in FLiNaK salt. A study by Qiu et al. showed that the main corrosion product of chromium was in trivalent form (in a complex K_2NaCrF_6) and showed the stability of Cr(III) because of the strong basic solvent properties of the FLiNaK salt, leading to the disproportionation of Cr(II) [20]. In the case of pure LiF salt, CrF$_3$ was found to be unstable [21]. CrF$_2$ shows higher stability in the latter salt, but the phase equilibria and solubility of CrF$_2$ in LiF salt were never investigated to this date.

In this work, different synthesis methods of chromium difluoride were explored. The phase equilibria in the binary systems LiF−CrF$_2$, CrF$_2$−ThF$_4$, and the ternary LiF-CrF$_2$−ThF$_4$ system, were then assessed experimentally. Based on these results, thermodynamic CALPHAD models based on the quasichemical model in the quadruplet approximation for the liquid solution were developed for the first time.

2. Experimental

2.1. Sample preparation

2.1.1. Starting materials

LiF (99.99%), CrF$_3$ (99.98%), and chromium powder (99.8%, 1250 mesh) (see, Table 1) were provided by Alfa Aesar, and dried in a furnace under argon at 573 K for 8 h. ThF$_4$ was synthesized at the Joint Research Center in Karlsruhe, using the process developed in-house by Souček et al. [22], consisting of the fluorination of ThO$_2$ with HF gas at 873 K.

The purity was controlled by X-ray Diffraction (XRD) analysis and by Differential Scanning Calorimetry (DSC) measurement (these techniques are described in further details in Sections 2.2 and 2.3, respectively). The XRD spectrum of ThF$_4$ confirmed the monoclinic structure (C2/c) of the product, while the DSC data indicated a melting temperature of (1387 ± 5) K, in good agreement with the data of Souček

et al., (1384.6 ± 5) K. Pure LiF was found to melt at (1124 ± 5) K, in close agreement with the melting temperature measured by Capelli et al. [23], i.e. 1119 K, and its diffractogram showed a cubic structure (Fm$\bar{3}$m), corroborating the purity of the chemical. The XRD and DSC analyses of CrF$_2$ are detailed in Section 4.1.

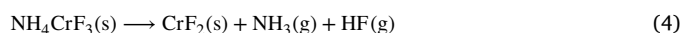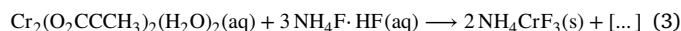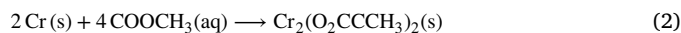#### 2.1.2. CrF$_2$ synthesis: CrF$_3$ reduction on chromium metal

It is challenging to prepare CrF$_2$ at high purity by the reaction of gaseous HF on metallic chromium [24,25], as handling HF gas is hazardous, and the process is not very effective. Two methods were used to synthesize pure CrF$_2$ in this work. The first one consisted in a reduction of pure CrF$_3$ powder on an excess of pure chromium powder, i.e. (Cr:CrF$_3$)=(1.25:2), according to the reaction below:

$$Cr^0(s) + 2\,CrF_3(s) = 3\,CrF_2(s) \tag{1}$$

Limited to small batches, i.e. 100 to 150 mg, the powders were thoroughly mixed and placed in a boron nitride liner, itself contained in a closed stainless steel crucible. The mixture was heated under argon atmosphere at 1053 K for 60 h with a heating and cooling rates of 5 K min^{-1} in a ceramic tubular furnace. The product was manually re-grinded in a mortar and heated using the same procedure twice more to a final mass yield of around 74%. The mass loss is due to the dispersion of the material during the grinding phases, to adhesion to the surface of the boron nitride liner, and formation of chromium gaseous phases (such as CrF$_5$). The final product was a dark green powder.

2.1.3. CrF$_2$ synthesis: Solution route

A second method was developed in order to get better repeatability. Inspired by the method reported by de Kozak [26], but simplified, the synthesis route consists in 3 steps given by the following reactions:

$$2\,Cr(s) + 4\,COOCH_3(aq) \longrightarrow Cr_2(O_2CCCH_3)_2(s) \tag{2}$$

$$Cr_2(O_2CCCH_3)_2(H_2O)_2(aq) + 3\,NH_4F \cdot HF(aq) \longrightarrow 2\,NH_4CrF_3(s) + [\ldots] \tag{3}$$

$$NH_4CrF_3(s) \longrightarrow CrF_2(s) + NH_3(g) + HF(g) \tag{4}$$

Firstly, reproducing the chromium tetraacetate synthesis route developed by Levy et al. [27], 8 grams of chromium metal powder were placed in a 200 mL solution of acetic anhydride and acetic acid (ratio 1:4) in a round flask equipped with a stirring bar and a hot plate under an argon atmosphere. Immediately, 4.5 ml of hydrobromic acid (HBr) were added to the solution. The mixture was then heated up to 598 K (225 °C) for 45 min at reflux. A brown precipitate was formed after the solution was cooled down to room temperature. This precipitate was cleaned twice with deoxygenated acetone, and was recovered by filtration under inert atmosphere (Fig. 1(a)).

In the second step, the anhydrous dichromium(II) tetraacetate (Cr$_2$(O$_2$CCCH$_3$)$_2$) obtained was dissolved into 50 mL of deoxygenated distilled water in a polycarbonate vial under argon atmosphere. 35 mL of ammonia and then 26 mL of hydrofluoric acid were progressively diluted in 50 mL degassed distilled water in another polycarbonate vial. This solution was heated up to 323 K (50 °C) and quickly injected in the dichromium(II) tetraacetate solution under intensive stirring. A light blue precipitate was formed after a few seconds. After two successive decanting steps with 50 mL of a 1:1 deoxygenated water/methanol solution and then 50 mL of pure methanol, the product was filtered under vacuum. The final product was a pale blue powder (Fig. 1(b)). It should be stressed that this product is not air sensitive, but was still maintained under argon atmosphere during storage and further handling.

The final step was based on de Kozak's recommendation [26]: a thin layer (2 to 4 mm high) of NH$_4$CrF$_3$ powder was placed inside an alumina boat in batches of about 200 mg and placed in a ceramic furnace under argon atmosphere. The thermolysis was carried out at a temperature of 873 K (600 °C) for 1 h, with a heating rate of 5 K min^{-1}. A pale green powder was obtained thereafter (Fig. 1(c)). It should be noted that larger batches can be used for this step, as long as the powder layer remains thin in the crucible. When using a thicker layer, formation of impurities such as Cr$_2$F$_5$ was observed.
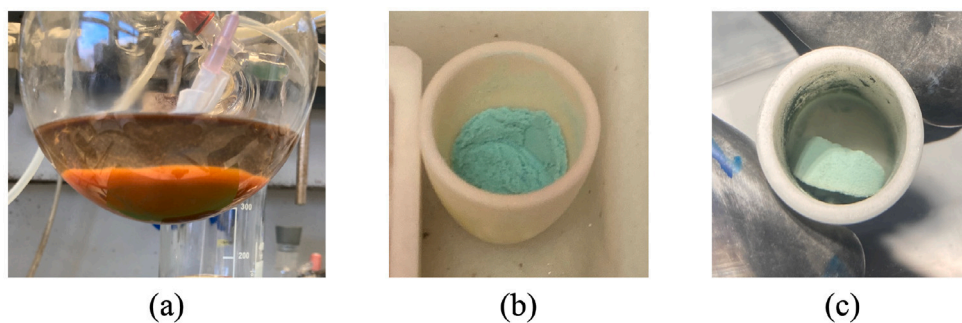
Fig. 1. The products obtained at every step of the synthesis, (a) $Cr_2(O_2CCCH_3)_2$ precipitate in acetone cleaning solution, (b) NH_4CrF_3 dry powder, and (c) CrF_2 powder.

2.2. X-ray diffraction

The purity of the pure compounds used in this work as starting material for the measurements and synthesis, were checked using X-ray Diffraction (XRD) at room temperature (T = 293 ± 2 K). For the inactive samples, a PANalytical X'Pert PRO X-ray diffractometer with a Cu anode (0.4 × 12 mm line focus, 45 KV, 40 mA) was used. Samples were homogeneously placed on a sample holder closed by a Kapton® film under argon atmosphere. X-ray data were collected by step scanning in the range $10° < 2\theta < 120°$ in a Bragg–Brentano configuration. The X-ray scattered intensities were measured with a real time multi strip (RTMS) detector (X'Celerator). For the active samples containing thorium, the X-ray measurements were performed using a Bruker D8 X-ray diffractometer mounted in a Bragg–Brentano configuration with a curved Ge monochromator (1, 1, 1) and a ceramic copper tube (40 kV, 40 mA), equipped with a LinxEye position-sensitive detector. The device was installed in a glovebox under inert nitrogen atmosphere. The purities of each powder was analyzed by Rietveld refinement method using the FullProf suite software [28,29].

2.3. Calorimetry measurements

Thermogravimetric measurements were conducted using a Netzsch STA 449C apparatus to assess the decomposition of NH_4CrF_3. The temperature was controlled by a Pt-Rh (10%) thermocouple. The measurements were made on powder samples (10–20 mg) up to 873 K in alumina crucibles, and the applied heating and cooling rates were 5 K min^{-1}.

3D heat flux Differential Scanning Calorimetry (DSC) measurements were conducted on a Setaram Multi Detector HTC module of the 96 line calorimeter. Every measurement consisted of at least four consecutive heating cycles with 5 or 10 K min^{-1} heating rates, and cooling rates of 5 to 10 K min^{-1}. The solidus and eutectic transition temperatures were extracted on heating, from the onset of the linear integration of the corresponding endothermic heat flow peak, while the liquidus transition temperatures were taken from the maximum of the corresponding peak according the NIST recommendations [30]. A correction was applied on the measured temperatures using a calibration equation determined with pure metals (Sn, Pb, Al, Ag, Au), as function of the heating rate. The uncertainties on the measurements are estimated at 5 K for the solidus and eutectic transitions, and 10 K for the liquidus transitions (because of the broader nature of the heat flow profile). The data retained for the phase equilibria determination were the ones collected on heating. The data collected on cooling were used as a more sensitive quality check for the amount of equilibria. The samples were prepared from the LiF, CrF_2 and ThF_4 end-member powders, closely mixed at the desired molar composition and inserted in a pure nickel liner. The liners were hermetically closed in stainless steel crucibles designed according to the concept developed at the Joint Research Centre in Karlsruhe [31], ensuring the stability of the samples' compositions and limiting the vapor releases during heating. The data collected in this work for the $LiF–CrF_2$, $CrF_2–ThF_4$, and $LiF–CrF_2–ThF_4$ systems are listed in Tables 5, 6 and 8, respectively.

2.4. Low-temperature heat capacity of CrF_2

Low-temperature heat capacity measurements were performed on the synthesized CrF_2 material, using a thermal-relaxation method [32] on $m = (1.83 ± 0.05)$ mg and $(6.35 ± 0.05)$ mg pellets in the temperature range T = (1.9–389) K, with a PPMS (Physical Property Measurement System, Quantum Design) instrument. Measurements were done both with no applied magnetic field ($B = 0$ T), and under magnetic field ($B = 1, 4, 6, 8, 10, 12, 14$ T), so as to get more insight into the origin of the anomaly observed around 49 K. The contributions of the sample platform, wires, and grease were obtained by a separate measurement of an addenda curve. The collected data on both pellets are listed in the Supplementary Information. Based on previous works with this instrument with standard materials, metallic, and oxide compounds, the uncertainty was estimated to be around 1%–2% in the middle range of acquisition (from 10 to 70 K), and around 3%–4% near room temperature and towards the lowest temperatures.

2.5. Magnetization measurements on CrF_2

Magnetization measurements were carried out in the temperature range T = (2–300) K and in magnetic fields up to 70 kOe using a SQUID-VSM instrument (MPMS3, Quantum Design). Due to the sensitivity of the material to air and moisture, encapsulation of the sample ($m = 32.4 ± 0.2$ mg) was performed in a dry air plexiglas container. The latter was calibrated beforehand, and its magnetic contribution was fitted with high precision (better than 5%). Measurements obtained by the VSM technique, i.e. DC magnetization (M), allowed us to derive DC magnetic susceptibility M/H (with H the applied magnetic field). AC magnetic measurements were moreover performed around the magnetic transition in 0 DC field, with an AC excitation field of 10 Oe at 35.798 Hz. The reader is referred to Appendix A and Supplementary Information for further details on the measurement results.

3. Thermodynamic modeling

The phase diagrams reported herein were modeled using the Fact-Sage software version 8.2 [33], based on the CALPHAD (CALculation of PHAse Diagrams) methodology [34,35]. The different parameters of the Gibbs energy functions of the $LiF–CrF_2$, $CrF_2–ThF_4$, and $LiF–CrF_2–ThF_4$ systems were optimized based on the experimental data collected in this work (see Sections 4.3 and 4.4). The parameters of the $LiF–ThF_4$ system, used to perform the modeling in the ternary system, were taken from Ocádiz et al. [36]. This model was based on experimental data from prior works of Thoma et al. and Capelli et al. [23,37,38].

Table 2

Thermodynamic and structural data for end-members and intermediate compounds used in this work for the thermodynamic assessment. Standard enthalpy of formation $\Delta_f H_m^o$(298.15 K), standard entropy S_m^0(298.15 K) and heat capacity coefficient of pure compounds $C_{p,m}$(T/K)/(J K^{-1} mol^{-1})= a + b·T + c·T^2 + d·T^{-2}.

Compound	Space group	$\Delta_f H_m^0$(298.15 K)	S_m^0(298.15 K)	$C_{p,m}$(T/K)/(J K^{-1} mol^{-1})= a + b·T + c·T^2 + d·T^{-2} + e·T^3				T(K)	Ref.
		(kJ mol^{-1})	(J K^{-1} mol^{-1})	a	b	c	d		
LiF$_{(cr)}$	Fm-3m(225)	−616.931	35.66	43.30898	1.6312168·10^{-2}	5.0470398·10^{-7}	−5.691236·10^5	298.15–2500	[42]
LiF$_{(l)}$		−598.654	42.96	64.183	–	–	–	298.15–6000	[42]
CrF$_{2(cr)}$	P2$_1$/c(14)	−781.800	86.87	76.68345	1.054105·10^{-2}	−1.386756·10^{-9}	−1.338373·10^6	298.15–1167	[41]
CrF$_{2(l)}$		−764.692	86.31	100	–	–	–	298.15–4000	[41]
ThF$_{4(cr)}$	C2/c(15)	−2097.900	142.05	111.46	2.69·10^{-2}	–	−7.8·10^5	298.15–2500	[36,43,44]
ThF$_{4(l)}$		−2100.360	106.61	168.0	–	–	–	298.15–2500	[36,43,44]
Li$_3$ThF$_{7(cr)}$	Ccca(68)	−3960.000	248.9	241.387	7.5836·10^{-2}	1.5141·10^{-6}	−2.4873·10^6	298.15–2500	[23,36]
LiThF$_{5(cr)}$	I4$_1$/a(88)	−2720.300	179.1	167.8	2.7·10^{-2}	–	−1.513510·10^6	298.15–2500	[23,36]
LiTh$_2$F$_{9(cr)}$	P4/nmm(129)	−4820.200	324.29	291.3	3.86·10^{-2}	–	−3.076934·10^6	298.15–2500	[23,36]
LiTh$_4$F$_{17(cr)}$	I4/m(87)	−9016.100	609.0	536.2	6.22·10^{-2}	–	−5.051854·10^6	298.15–2500	[23,36]

3.1. Gibbs energies of pure compounds

For pure compounds, the Gibbs energy is expressed by:

$$G(T) = \Delta_f H_m^o(298.15) - S_m^o(298.15) \cdot T + \int_{298.15}^{T} C_{p,m}(T)dT - T \int_{298.15}^{T} \frac{C_{p,m}}{T} dT \tag{5}$$

where $\Delta_f H_m^o$(298.15) is the standard enthalpy of formation, and S_m^o(298.15) is the standard entropy of the pure compound at standard pressure and reference temperature 298.15 K. $C_{p,m}$ is the heat capacity defined as:

$$C_{p,m}(T) = a + bT + cT^2 + dT^{-2} \tag{6}$$

The thermodynamic data for LiF were taken from the JRCMSD database [39], and from the re-evaluation of Tosolin et al. for ThF$_4$ [36, 40]. For CrF$_2$, the thermodynamic functions were taken from the IVTAN database [41]. All the thermodynamic data used in this work are summarized in Table 2.

3.2. Liquid solution

The modified quasichemical model in the quadruplet approximation was used to describe the liquid solutions [45,46]. This model describes well ionic liquids with strong short-range ordering. The basic unit of the liquid solution in this model is a quadruplet composed of two anions (F$^-$ twice in this case) and two cations (A^{n+} and B^{m+}). The composition of maximum short-range ordering in this model is selected by varying the ratio between the cation–cation coordination numbers $Z_{AB/FF}^A$ and $Z_{AB/FF}^B$.

Two interactions are considered: the First Nearest Neighbor (FNN) interaction (cation - anion interaction) and the Second Nearest Neighbor (SNN) interaction (interactions between the two nearest ions in the same sublattice). Short-range ordering is defined by the quadruplet approximation and includes the SNN interactions between each cation and each anion. Here, $\Delta g_{AB/F}$ is defined as the parameter of the Gibbs energy change associated with the SNN exchange reaction described as:

$$\Delta g_{AB/F} = \Delta g_{AB/F}^0 + \sum_{i\geq 1} g_{AB/F}^{i0} \chi_{AB/F}^i + \sum_{j\geq 1} g_{AB/F}^{0j} \chi_{BA/F}^j \tag{7}$$

where $\Delta g_{AB/F}^0$ and $g_{AB/F}^{ij}$ can be dependent on temperature, but independent of composition. These parameters are optimized to match as best as possible the experimental data available for each system. The dependence on composition is given by the term $\chi_{AB/F}$ defined as:

$$\chi_{AB/F} = \frac{X_{AA}}{X_{AA} + X_{AB} + X_{BB}} \tag{8}$$

where X_{AA}, X_{AB} and X_{BB} represent the different cation–cation pair fractions. The anion–anion coordination is then calculated such

Table 3

Cation–cation and anion–anion coordination numbers of the liquid solution used in this work for the thermodynamic modeling.

A	B	$Z_{AB/FF}^A$	$Z_{AB/FF}^B$	$Z_{AB/FF}^F$
Li$^+$	Li$^+$	6	6	6
Cr^{2+}	Cr^{2+}	6	6	3
Th^{4+}	Th^{4+}	6	6	1.5
Li$^+$	Cr^{2+}	6	6	4
Li$^+$	Th^{4+}	2	6	1.71
Cr^{2+}	Th^{4+}	2	6	1.2

that electro-neutrality in the system is maintained. The selection of anion–anion coordination is made according to the following equation:

$$\frac{q_A}{Z_{AB/FF}^A} + \frac{q_B}{Z_{AB/FF}^B} = 2 \cdot \frac{q_F}{Z_{AB/FF}^F} \tag{9}$$

where q_i represent the charges of the different ions, and $Z_{AB/FF}^F$ represents the anion–anion coordination number. The ratio of cation–cation coordination numbers $Z_{AB/FF}^A$ and $Z_{AB/FF}^B$ is selected to match the composition of maximum short-range ordering, usually found close to the lowest eutectic in the phase diagrams, where the Gibbs energy is expected to reach its minimum. The coordination numbers selected in this work are listed in Table 3.

The optimized excess Gibbs energies for the LiF−CrF$_2$ and CrF$_2$−ThF$_4$ binary systems of the liquid solutions are given by the following equations:

$$\Delta g_{LiCr/FF} = -4993 + (-600 + 2.75 \cdot T)\chi_{LiCr/FF} + (279 + 3.2 \cdot T)\chi_{CrLi/FF} \quad \text{J mol}^{-1} \tag{10}$$

$$\Delta g_{CrTh/FF} = -669 + (-5045 + 5 \cdot T)\chi_{CrTh/FF} + (-3531 + 7 \cdot T)\chi_{ThCr/FF} \quad \text{J mol}^{-1} \tag{11}$$

These equations were optimized by manual iteration with support from the FactSage Calphad Optimizer version 1.3. For the LiF−ThF$_4$ system, the equation and intermediate compounds data were taken from Ocadiz et al. [36]. The optimized excess Gibbs energy parameters are reproduced here for completeness.

$$\Delta g_{LiTh/FF} = -10878 + (-6694 + 2.929 \cdot T)\chi_{LiTh/FF} + (-20920 + 19.25 \cdot T)\chi_{ThLi/FF} \quad \text{J mol}^{-1} \tag{12}$$

3.2.1. Liquid solution for the ternary system

The ternary phase diagram of the LiF−CrF$_2$−ThF$_4$ system was calculated from the three binary sub-systems described above, using the Kohler/Toop interpolation [47]. This is an asymmetric interpolation model for which two symmetry groups are considered: LiF belongs to the first group of symmetry, i.e. the monovalent group, which tends to remain a dissociated ionic liquid; CrF$_2$ (divalent) and ThF$_4$ (tetravalent) belong to the second group of symmetry, which is more apt to form
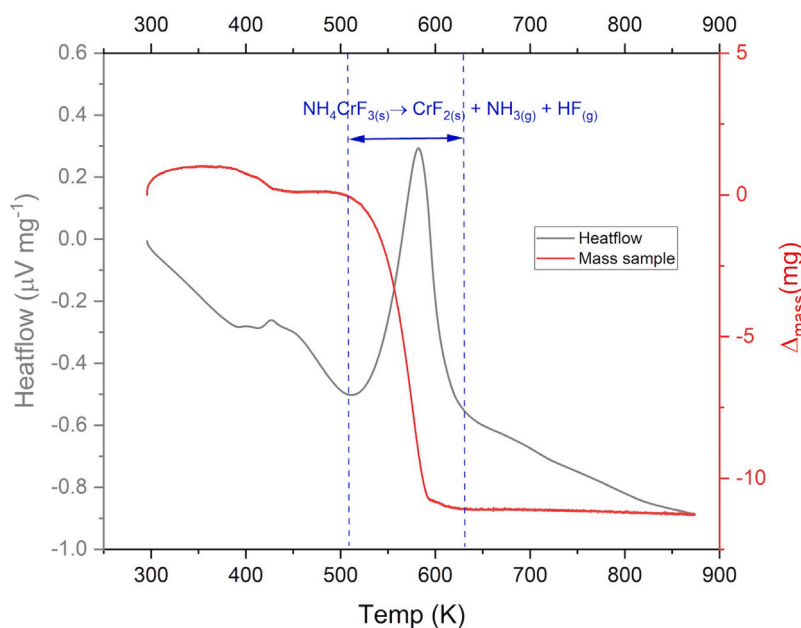
Fig. 2. TGA profile of the decomposition of NH_4CrF_3 under a 5 K min⁻¹ heating from 293 to 873 K under argon flow.

molecular species in the melt. No ternary excess parameter was needed to describe the phase equilibria in the ternary system. Based on the binary models optimized here, the experimental ternary data were found in sufficient agreement without any excess term (see Section 4.4).

4. Results & discussions

4.1. CrF_2 synthesis and product characterization

Using the first synthesis route, i.e. reduction of CrF_3 mixed with Cr metal, the product purity after 3 cycles was determined at $(99 \pm 1)\%$ based on Rietveld refinement of the XRD data, and the melting temperature measured at (1164 ± 5) K by DSC, in good agreement with literature data from Sturm [48]: (1167 ± 6) K. Impurities of CrF_3 and Cr_2F_5 were still detected in the XRD measurement. We hypothesize that the excess of Cr^0 mainly diffused into the porosity of the boron nitride liner.

Using the second synthesis route, i.e. in solution, the final product purity was determined to be $(99.5 \pm 0.5)\%$, based on the combined XRD and DSC data. No secondary phases were detected, and the melting temperature of the compound was measured at (1167 ± 5) K, in excellent agreement with the measurement of Sturm [48]. In the intermediate steps, the formation of NH_4CrF_3 dry powder was also confirmed by XRD. A Thermal Gravimetric Analysis (TGA) showed that total vaporization of $NH_3(g)$ and $HF(g)$ occurs during the thermolysis at a temperature of 633 K (360 °C) (see Fig. 2). The temperature selected in the synthesis was 873 K (600 °C) so as to ensure a high crystallinity of the final product.

On the basis of the success of the second method, the mass yields and purities of the final products, the synthesis route in solution was considered more robust overall. CrF_2 crystallizes with monoclinic symmetry, in space group $P2_1/c$ (see Fig. 3). The refined lattice parameters and atomic positions obtained in this work are listed in Table 4.

4.2. CrF_2 low-temperature heat capacity

Using the high purity material prepared with the solution route, low temperature heat capacity measurements were conducted using thermal relaxation calorimetry in the range (1.9–389) K. The data collected in this work are found in very good agreement with the data

reported in 1979 by Boo and Stout [49] in the temperature range (10–300 K) using adiabatic calorimetry (see Figs. 4). The present data extend the range of temperature from (1.9–10 K) and (300–389 K), respectively. Boo and Stout [49] performed a very thorough analysis of the heat capacity of this compound, including with the accounting of Cr^{2+} crystal field electronic ground state contribution. In accordance with Lim and Stout [50,51], the authors report a ligand field of D_{4h} symmetry, a $^5B_{1g}$ ground orbital level, and a low-lying orbital level $^5A_{1g}$ at 116 cm⁻¹. We retain here the standard entropy value recommended by the authors at 86.87 J·K⁻¹·mol⁻¹ for the thermodynamic modeling assessment.

It is also worth pointing out that the measured data above 300 K (estimated to have a 3%–4% uncertainty) is in good agreement with the heat capacity function recommended in the IVTAN tables [41], as shown in Fig. A.2 in Appendix A, supporting the selection of thermodynamic data.

Moreover, the magnetic anomaly reported by Boo and Stout [49] around (49.26 ± 0.01) K is confirmed with our heat capacity data, although the shape of the λ anomaly is not as sharp. Nevertheless, we can confirm the antiferromagnetic nature of the magnetic transition, as the anomaly shifts to slightly lower temperatures upon application of a magnetic field (see Fig. A.1 in Appendix A). Complementary magnetization studies were then performed, as detailed in Appendix B and in the Supplementary Information, to get more insight into the magnetic properties of this compound.

4.3. Binary systems

4.3.1. $LiF-CrF_2$

The phase equilibria measurements on this system do not indicate the presence of any stable intermediate compound. Only thermodynamic equilibria identified as eutectic and liquidus transitions were observed. X-ray Diffraction analyses performed after DSC measurements showed only XRD patterns of LiF and CrF_2 end-members. The consistency of the solidus line temperatures measured along all the range of compositions, and the logical liquidus trend confirmed this hypothesis. A unique eutectic equilibrium was measured at $X_{CrF_2} = 0.45$ and at a temperature of (822 ± 5) K. The model was optimized based on the measured experimental data (Table 5, Fig. 5).
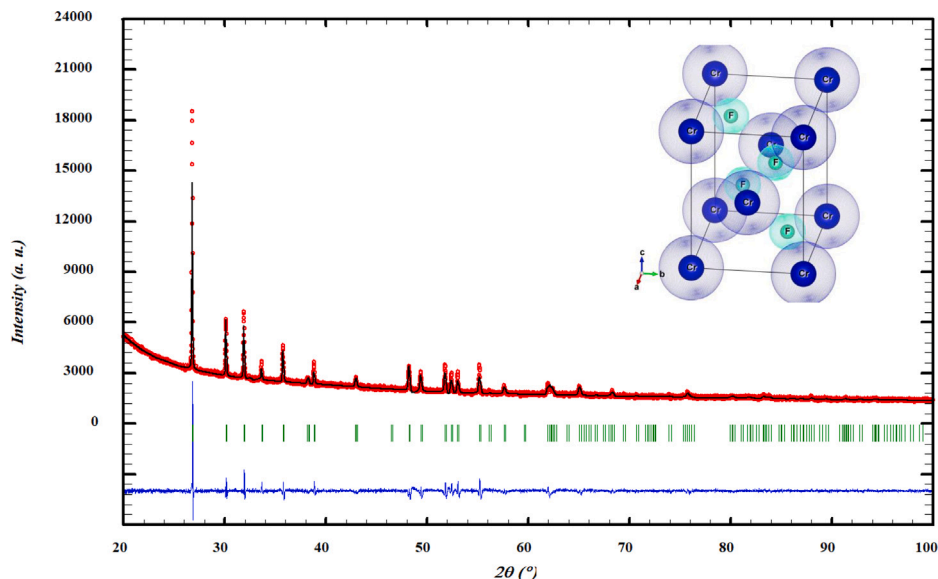
Fig. 3. Diffractogram of CrF$_2$ synthesized by the solution route Y$_{obs}$ (red dots), measured at (293 ± 2) K with a Cu anode, compared to the Rietveld refinement performed on the FullProf suite software. Y$_{calc}$ (black line) is the calculated XRD pattern; Y$_{obs}$ - Y$_{calc}$ (blue line) is the differential calculation between observed and calculated data. The Bragg's reflection angular positions of CrF$_2$ are shown by green marks. The inset shows a schematic representation of the unit cell. Cr atoms are shown in blue, while fluorine atoms are shown in light green.
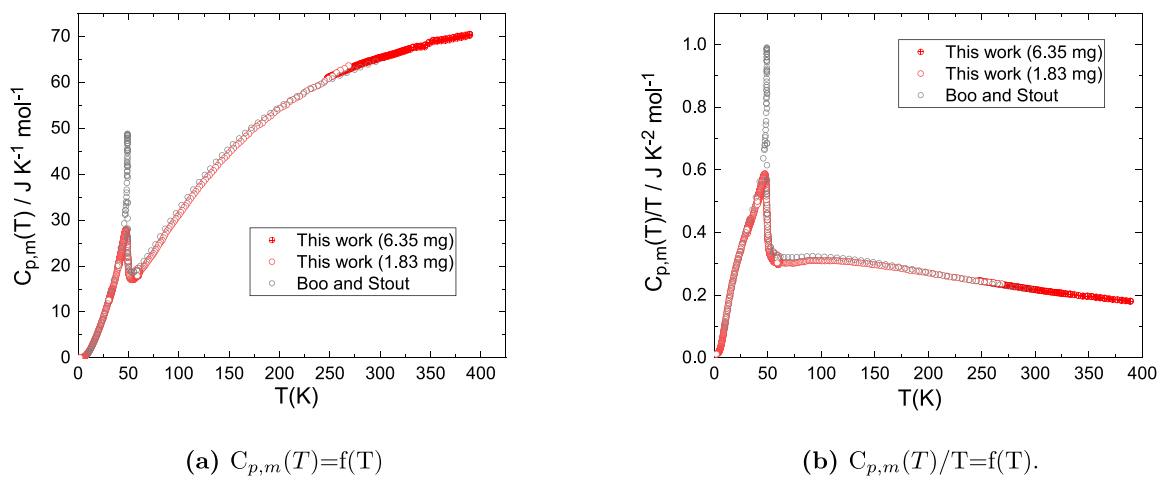

(a) C$_{p,m}(T)$=f(T)

(b) C$_{p,m}(T)$/T=f(T).

Fig. 4. Heat capacity of CrF$_2$ measured in this work, and compared to the data measured by Boo and Stout [49].

Table 4
Refined lattice parameters and atomic positions for CrF$_2$, obtained in this work by the solution route. CrF$_2$ crystallizes with monoclinic symmetry, in space group P2$_1$/c (space group 14).

Lattice parameters	a(Å)	b(Å)	c(Å)	Angle β (°)
	3.5132(1)	4.7131(2)	5.5650(2)	122.413(1)
Atomic positions	Wyck.	x	y	z
Cr	2a	0	0	0
F	4e	0.259(2)	0.303(1)	0.308(1)

4.3.2. CrF$_2$-ThF$_4$

As for the system described above, the calorimetry measurements showed a consistent eutectic temperature for all the range of compositions. The liquidus transitions were also in-line with a simple eutectic system. The XRD spectra collected for different representative compositions settled that the mixtures were composed of CrF$_2$ and ThF$_4$ only. The eutectic composition was not measured directly. The measurement at the composition X$_{CrF_2}$ = 0.324, showed only one transition at a

temperature of (1034 ± 5) K on the heating curve. However, the cooling curve showed clearly the presence of a liquidus/solidification peak at a higher temperature, which was too close to be differentiated on the heating curve. The phase diagram was modeled on the basis of the collected data, with an eutectic composition calculated at X$_{CrF_2}$ = 0.31 (see Table 6 and Fig. 6).

4.4. Ternary system LiF-CrF$_2$-ThF$_4$

The initial phase diagram calculation of the ternary system was based on the three binary models: LiF−CrF$_2$, CrF$_2$−ThF$_4$, and LiF−ThF$_4$ (optimized by Ocádiz et al. [36]) (see Table 7). Based on this model, experimental data were collected at different compositions selected on the isopleth sections with 10% and 20% CrF$_2$ (see Table 8). A last experimental measurement was made at the composition LiF−CrF$_2$−ThF$_4$ (0.20−0.60-0.20), so as to get a more detail impression of the ternary phase diagram. The results are listed in Table 8.

The collected experimental data, projected on the isopleth section 0.9 (LiF−ThF$_4$)+ 0.1 CrF$_2$, show a very good agreement with the
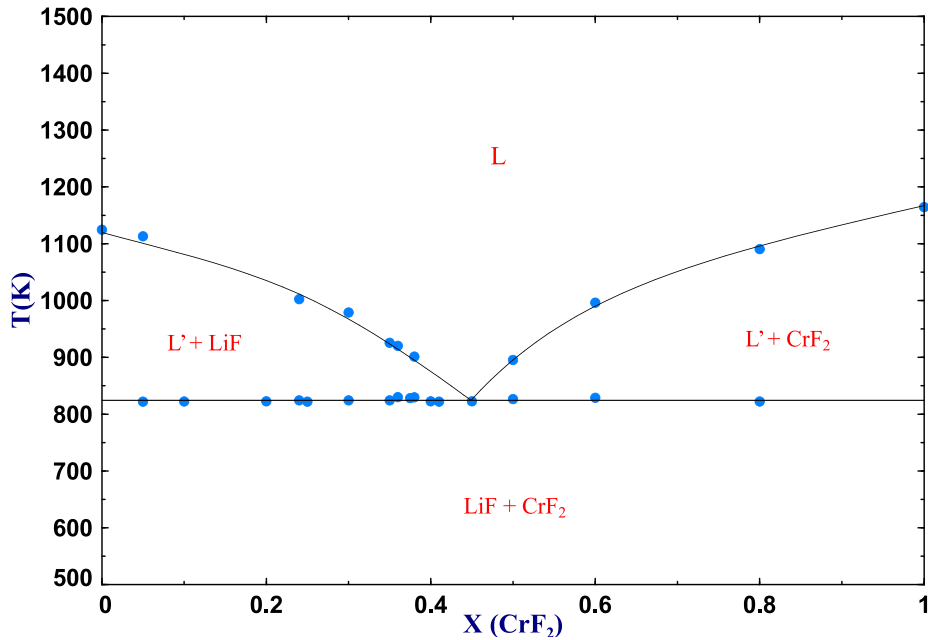
Fig. 5. Phase diagram of the LiF–CrF$_2$ system, blue circles (●) represent the experimental data collected in this work (Table 5).

Table 5
Phase diagram equilibria in the LiF–CrF$_2$ system collected by DSC in this work.

X_{LiF}	X_{CrF_2}	T (K)	Equilibrium	Reaction	X_{LiF}	X_{CrF_2}	T (K)	Equilibrium	Reaction
1	0	1124.3	Melting	LiF = L	0.625	0.375	828	Eutectic	LiF + CrF$_2$ = L
0.95	0.05	822	Eutectic	LiF + CrF$_2$ = L	0.625	0.375	877	Liquidus	LiF + L' = L
0.95	0.05	1113	Liquidus	LiF + L' = L	0.62	0.38	829	Eutectic	LiF + CrF$_2$ = L
0.90	0.10	822	Eutectic	LiF + CrF$_2$ = L	0.62	0.38	901	Liquidus	LiF + L' = L
0.80	0.20	822	Eutectic	LiF + CrF$_2$ = L	0.60	0.40	822	Eutectic	LiF + CrF$_2$ = L
0.76	0.24	824	Eutectic	LiF + CrF$_2$ = L	0.59	0.41	822	Eutectic	LiF + CrF$_2$ = L
0.76	0.24	1002	Liquidus	LiF + L' = L	0.55	0.45	822	Eutectic	LiF + CrF$_2$ = L
0.75	0.25	822	Eutectic	LiF + CrF$_2$ = L	0.50	0.50	826	Eutectic	LiF + CrF$_2$ = L
0.70	0.30	824	Eutectic	LiF + CrF$_2$ = L	0.50	0.50	895	Liquidus	CrF$_2$ + L' = L
0.70	0.30	979	Liquidus	LiF + L' = L	0.40	0.60	829	Eutectic	LiF + CrF$_2$ = L
0.65	0.35	824	Eutectic	LiF + CrF$_2$ = L	0.40	0.60	996	Liquidus	CrF$_2$ + L' = L
0.65	0.35	926	Liquidus	LiF + L' = L	0.20	0.80	822	Eutectic	LiF + CrF$_2$ = L
0.64	0.36	830	Eutectic	LiF + CrF$_2$ = L	0.20	0.80	1090	Liquidus	CrF$_2$ + L' = L
0.64	0.36	920	Liquidus	LiF + L' = L	0	1	1164.2	Melting	CrF$_2$ = L

The uncertainties on the temperature measurement are estimated at ± 5 K for the melting and eutectic transitions, and ± 10 K for the liquidus transitions.

Table 6
Phase diagram equilibria in the CrF$_2$–ThF$_4$ system collected by DSC in this work.

X_{CrF_2}	X_{ThF_4}	T (K)	Equilibrium	Reaction	X_{CrF_2}	X_{ThF_4}	T (K)	Equilibrium	Reaction
1	0	1167.5	Melting	CrF$_2$ = L	0.468	0.532	1034	Eutectic	CrF$_2$ + ThF$_4$ = L
0.949	0.051	1027	Eutectic	CrF$_2$ + ThF$_4$ = L	0.468	0.532	1197	Liquidus	ThF$_4$ + L' = L
0.949	0.051	1050	Liquidus	CrF$_2$ + L' = L	0.443	0.557	1034	Eutectic	CrF$_2$ + ThF$_4$ = L
0.733	0.267	1034	Eutectic	CrF$_2$ + ThF$_4$ = L	0.443	0.557	1205.6	Liquidus	ThF$_4$ + L' = L
0.733	0.267	1055	Liquidus	CrF$_2$ + L' = L	0.367	0.633	1034	Eutectic	CrF$_2$ + ThF$_4$ = L
0.676	0.324	1034	Eutectic	CrF$_2$ + ThF$_4$ = L	0.367	0.633	1238	Liquidus	ThF$_4$ + L' = L
0.610	0.390	1034	Eutectic	CrF$_2$ + ThF$_4$ = L	0.316	0.684	1035	Eutectic	CrF$_2$ + ThF$_4$ = L
0.610	0.390	1106	Liquidus	ThF$_4$ + L' = L	0.316	0.684	1284	Liquidus	ThF$_4$ + L' = L
0.601	0.399	1034	Eutectic	CrF$_2$ + ThF$_4$ = L	0.104	0.896	1029	Eutectic	CrF$_2$ + ThF$_4$ = L
0.550	0.450	1034	Eutectic	CrF$_2$ + ThF$_4$ = L	0.104	0.896	1366	Liquidus	ThF$_4$ + L' = L
0.550	0.450	1121	Liquidus	ThF$_4$ + L' = L	0	1	1386.8	Melting	ThF$_4$ = L
0.504	0.496	1031	Eutectic	CrF$_2$ + ThF$_4$ = L					

The uncertainties on the temperature measurement are estimated at ± 5 K for the melting and eutectic transitions, and ± 10 K for the liquidus transitions.

model. The invariant equilibria are well reproduced, with reasonable discrepancies as seen in Fig. 7.

Even if the discrepancies are a bit more pronounced, in the 0.8 (LiF–ThF$_4$)+ 0.2 CrF$_2$ section, the agreement of the model with the experimental data is reasonably good (Fig. 8).

At LiF–CrF$_2$–ThF$_4$ (0.20-0.60-0.20) the three data points obtained fit almost perfectly with the calculated invariant equilibria (Fig. 9).

Post-XRD measurements of the calorimetric samples showed, once again, no evidence for the formation of an intermediate compound. Instead, the intermediates compounds of the LiF–ThF$_4$ system, in their
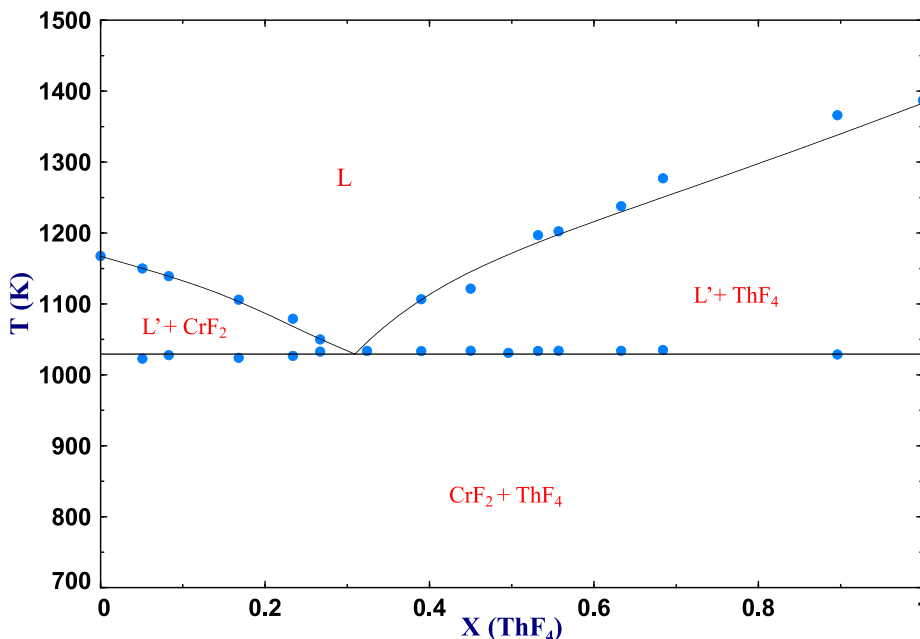
Fig. 6. Phase diagram of the CrF_2-ThF_4 system, blue circles (●) represent the experimental data collected in this work (Table 6).

Table 7
Invariant equilibria in $LiF-CrF_2$, $LiF-ThF_4$ and CrF_2-ThF_4 systems modeled in this work, compared to the measured data.

System	Invariant reaction	Equilibrium	Composition	Modeled temperature (K)	Measured temperature (K)
$LiF-CrF_2$	$LiF + CrF_2 = L$	Eutectic	$X_{CrF_2} = 0.45$	823	(822 ± 5)
$LiF-ThF_4$	$LiF + Li_3ThF_7 = L$	Eutectic	$X_{ThF_4} = 0.24$	835.8	(832 ± 5)[a]
	$Li_3ThF_7 = L$	Congruent melting	$X_{ThF_4} = 0.25$	836.9	(832 ± 5)[a]
	$Li_3ThF_7 + LiThF_5 = L$	Eutectic	$X_{ThF_4} = 0.28$	834.4	(826 ± 5)[a]
	$LiThF_5 = LiTh_2F_9 + L'$	Peritectic	$X_{ThF_4} = 0.50$	872.1	(870 ± 5)[a]
	$LiTh_2F_9 = LiTh_4F_{17} + L'$	Peritectic	$X_{ThF_4} = 0.67$	1036.3	(1038 ± 5)[a]
	$LiTh_4F_{17} = ThF_4 + L'$	Peritectic	$X_{ThF_4} = 0.80$	1173.8	(1176 ± 5)[a]
CrF_2-ThF_4	$CrF_2 + ThF_4 = L$	Eutectic	$X_{ThF_4} = 0.31$	1029	(1034 ± 5)

[a] The experimental data presented here were collected by Capelli et al. [23].

Table 8
Phase diagram equilibria of the $LiF-CrF_2-ThF_4$ system collected by DSC in this work.

X_{LiF}	X_{CrF_2}	X_{ThF_4}	T(K)	Model T(K)	Equilibrium	Reaction	X_{LiF}	X_{CrF_2}	X_{ThF_4}	T(K)	Model T(K)	Equilibrium	Reaction
0.80	0.10	0.10	761.7	761	eutectic	$LiF + CrF_2 + Li_3ThF_7 = L$	0.29	0.10	0.61	1182.1	1191	liquidus	$ThF_4 + L' = L$
0.80	0.10	0.10	966.9	981	liquidus	$L' + LiF = L$	0.60	0.20	0.20	760.5	761	eutectic	$LiF + CrF_2 + Li_3ThF_7 = L$
0.60	0.10	0.30	767.3	763	quasi-peritectic	$L + LiThF_5 = CrF_2 + Li_3ThF_7$	0.60	0.20	0.20	766.7	763	liquidus	$L'' + Li_3ThF_7 = L' \; LiF$
0.60	0.10	0.30	790.4	796	liquidus	$L'' + Li_3ThF_7 = L' + LiThF_5$	0.60	0.20	0.20	784.9	777	liquidus	$LiF + L' = L$
0.60	0.10	0.30	851.9	836	liquidus	$L'' + LiThF_5 = L' + LiTh_2F_9$	0.40	0.20	0.40	754.2	763	quasi-peritectic	$L + LiThF_5 = CrF_2 + Li_3ThF_7$
0.55	0.10	0.35	764.9	763	quasi-peritectic	$L + LiThF_5 = CrF_2 + Li_3ThF_7$	0.40	0.20	0.40	808.1	785	quasi-peritectic	$L + LiTh_2F_9 = CrF_2 + LiThF_5$
0.55	0.10	0.35	849.6	830	liquidus	$L'' + LiThF_5 = L' + LiTh_2F_9$	0.40	0.20	0.40	877.6	–	–	–
0.50	0.10	0.40	763.4	763	quasi-peritectic	$L + LiThF_5 = CrF_2 + Li_3ThF_7$	0.40	0.20	0.40	992.5	1045	liquidus	$LiTh_2F_9 + L' = L$
0.50	0.10	0.40	817.1	820	liquidus	$L'' + LiThF_5 = L' + LiTh_2F_9$	0.21	0.20	0.59	977.3	–	–	–
0.45	0.10	0.45	761.9	763	quasi-peritectic	$L + LiThF_5 = CrF_2 + Li_3ThF_7$	0.21	0.20	0.59	1231.5	1192	liquidus	$ThF_4 + L' = L$
0.45	0.10	0.45	804.6	805	liquidus	$L'' + LiThF_5 = L' + LiTh_2F_9$	0.20	0.60	0.20	796.9	785	peritectic	$LiThF_5 = CrF_2 + LiTh_2F_9 + L'$
0.45	0.10	0.45	810.4	805	–	–	0.20	0.60	0.20	914.9	926	liquidus	$LiTh_4F_{17} + L'' = L'$
0.45	0.10	0.45	1038.5	1080	liquidus	$L' + LiTh_4F_{17} = L$	0.20	0.60	0.20	1026.5	1015	liquidus	$CrF_2 + L' = L$

area of predominance, were detected, or the pure end-members in addition to CrF_2.

Based on the overall good agreement of the modeled ternary phase diagram with the experimental data, it appeared that no ternary excess parameter, i.e. no additional optimization, was needed. The final ternary phase diagram plotted as liquidus projection, is shown in Fig. 10 and the invariant equilibria are listed in Table 9. The systems displays one ternary eutectic, and four quasi-peritectic equilibria.

Several isotherms computed at T = 750, 850, 950, and 1050 K are also shown in Appendix in Appendix C.

Unlike CrF_3, CrF_2 does not form any intermediate compound with lithium fluoride [21]. In this work, it was demonstrated that it also remains soluble in molten $LiF-ThF_4$ solution. To assess the impact on the phase diagram equilibria of the $LiF-ThF_4$ molten salt system, computations were performed for several amounts of CrF_2 dissolved in the salt, and are shown in Fig. 11. As shown in Fig. 11(a), a 1%
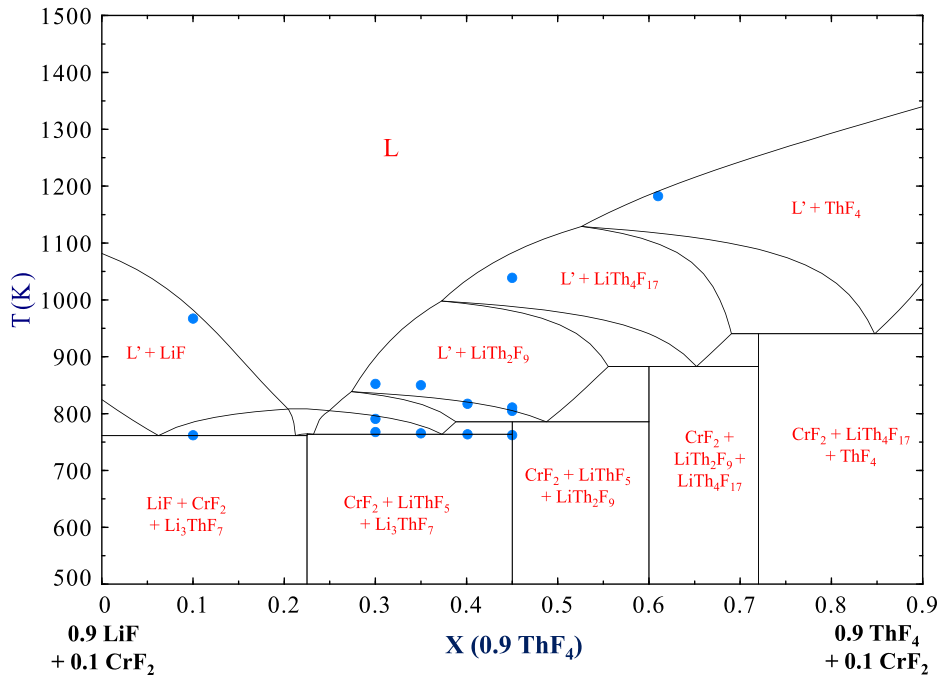
Fig. 7. Phase diagram of the isopleth 0.9 (LiF−ThF$_4$) + 0.1 CrF$_2$ section, blue circles (●) represent the experimental data collected in this work (Table 8). Note that for the composition X(0.9 ThF$_4$) = 0.61, 4 to 5 events were detected on the cooling curves as expected from the phase equilibria, but are not indicated here, as the derived temperatures were shifted due to undercooling effects.
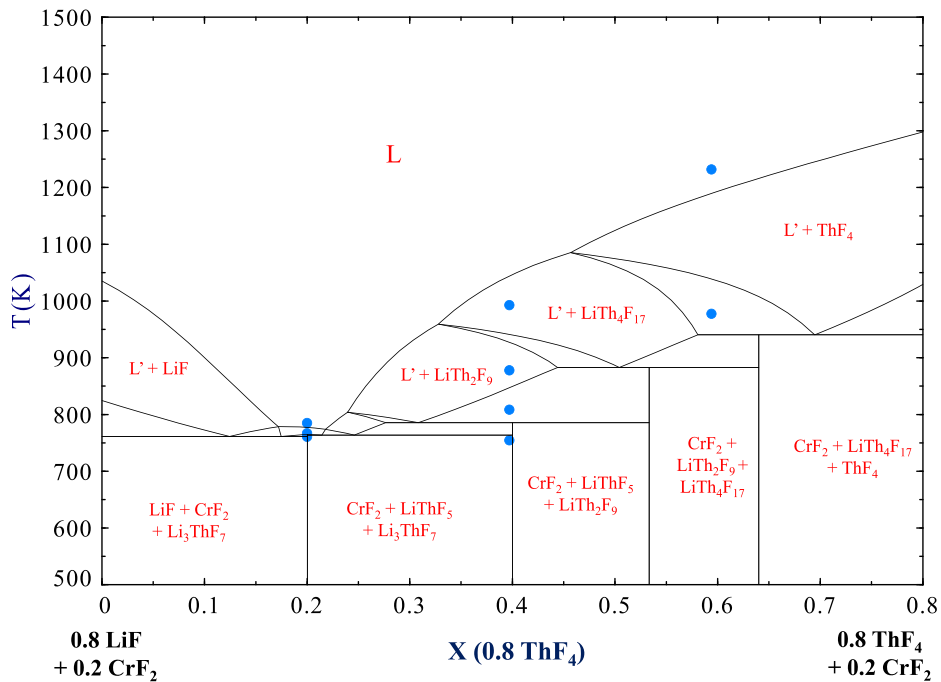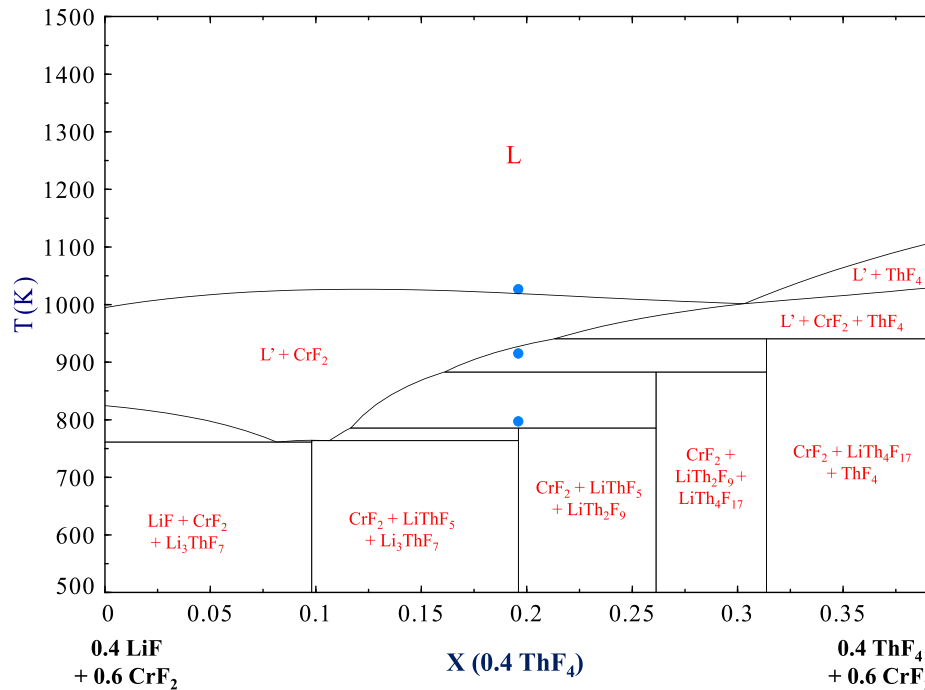

Fig. 8. Phase diagram of the isopleth 0.8 (LiF−ThF$_4$) + 0.2 CrF$_2$ system, blue circles (●) represent the experimental data collected in this work (Table 8).

Table 9
Invariant equilibria calculated for the LiF−CrF$_2$−ThF$_4$ system.

N°	X$_{LiF}$	X$_{CrF_2}$	X$_{ThF_4}$	T (K)	Invariant equilibrium	Reaction
1	0.245	0.464	0.291	940	Quasi-peritectic	L + ThF$_4$ = CrF$_2$ + LiTh$_4$F$_{17}$
2	0.375	0.365	0.261	883	Quasi-peritectic	L + LiTh$_4$F$_{17}$ = CrF$_2$ + LiTh$_2$F$_9$
3	0.529	0.247	0.224	785	Quasi-peritectic	L + LiTh$_2$F$_9$ = CrF$_2$ + LiThF$_5$
4	0.562	0.229	0.209	764	Quasi-peritectic	L + LiThF$_5$ = CrF$_2$ + Li$_3$ThF$_7$
5	0.594	0.250	0.156	761	Eutectic	CrF$_2$ + Li$_3$ThF$_7$ + LiF = L

Fig. 9. Phase diagram of the isopleth 0.4 (LiF−ThF$_4$) + 0.6 CrF$_2$ system, blue circles (●) represent the experimental data collected in this work (Table 8).
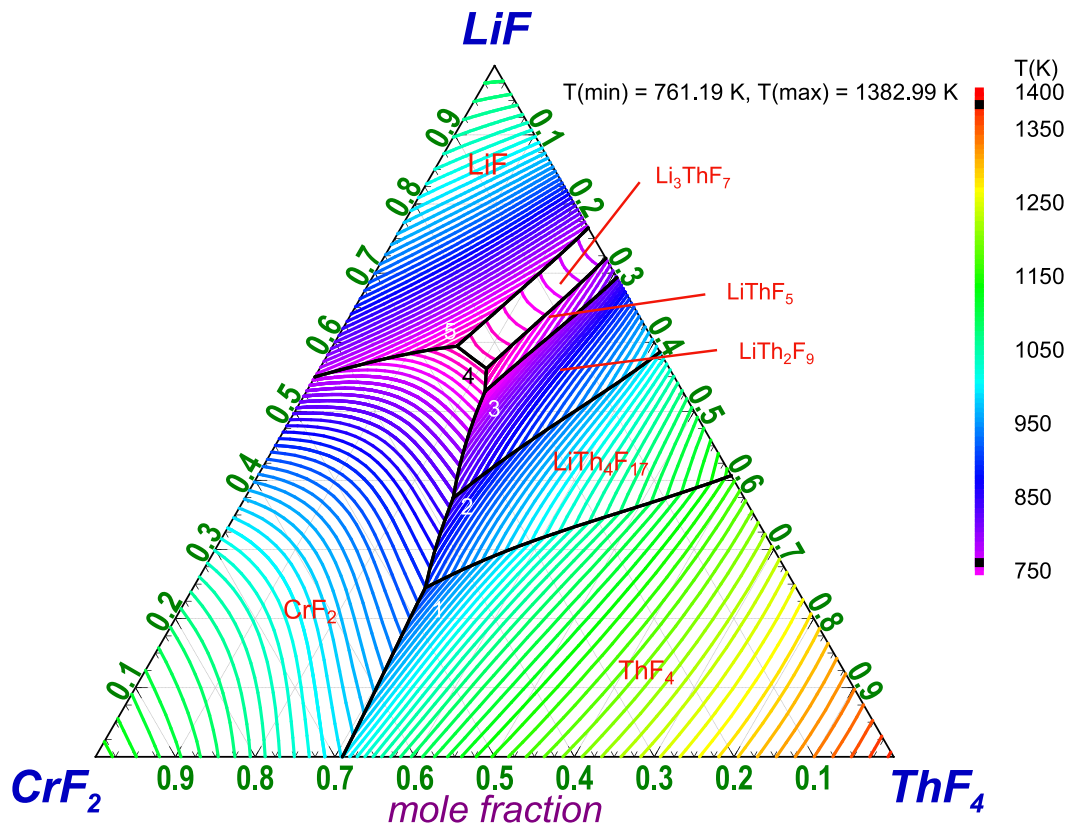

Fig. 10. Liquidus projection of the LiF−CrF$_2$−ThF$_4$ system calculated in this work from 750 K to 1400 K with an increment of 10 K. Primary crystallization fields are detailed in the figure.

addition of CrF$_2$ has very little impact on the phase equilibria, and thus on the thermodynamic behavior. In the case of a 15% addition, i.e. a large excess compared to what would be expected under operating conditions, a significant decrease in the liquidus temperature of approximately 70 K would occur. This information is fundamental to support the safety assessment of the Molten Salt Reactor. The stability of CrF$_2$
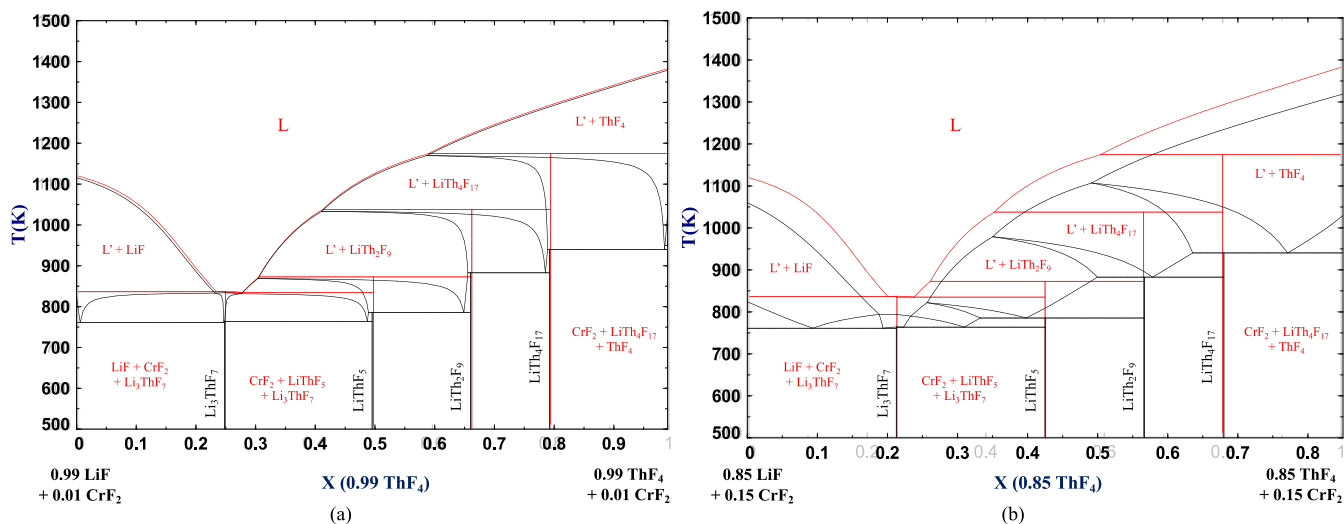
Fig. 11. Phase diagram of the pseudo-binary (a) 0.99 (LiF−ThF$_4$) + 0.01 CrF$_2$ and (b) 0.85 (LiF−ThF$_4$) + 0.15 CrF$_2$ systems, the binary phase diagram of the LiF−ThF$_4$ system, derived from the model of Ocádiz Flores et al. [36], is superimposed in red.

limits the risk of oxidation to CrF$_3$, and consequently the increase of the fluoroacidity, and further chromium depletion in the structural alloy, as reported by Liu et al. [11].

5. Conclusion

In this work, two methods are reported for the synthesis of pure CrF$_2$. Calorimetric measurements were moreover carried out for the first time in the LiF−CrF$_2$, CrF$_2$−ThF$_4$, and LiF−CrF$_2$−ThF$_4$ systems. Using the modified quasichemical model in the quadruplet approximation for the liquid solution, thermodynamic models of the aforementioned systems were then developed. CrF$_2$ does not form any quaternary intermediate compound in the molten LiF−ThF$_4$ system. This constitutes new knowledge for the safety assessment of the Molten Salt Reactor, especially related to the effect of corrosion products on the fuel salt behavior. The logic extension of this work is the consideration of the effect of UF$_4$ on the molten salt fuel, and its possible interaction with CrF$_2$ according to the reaction UF$_4$ + CrF$_2$ = UF$_3$ + CrF$_3$. Follow-up studies should also consider the influence of the ratio UF$_4$/UF$_3$ and redox equilibria with the CrF$_2$/CrF$_3$ couple.

CRediT authorship contribution statement

T. Dumaire: Writing – review & editing, Writing – original draft, Methodology, Investigation, Formal analysis, Data curation, Conceptualization. **O. Walter:** Writing – review & editing, Resources, Methodology, Investigation. **O. Beneš:** Writing – review & editing, Supervision, Methodology. **J.-C. Griveau:** Writing – review & editing, Investigation, Formal analysis, Data curation, Conceptualization. **E. Colineau:** Writing – review & editing, Investigation, Formal analysis, Data curation, Conceptualization. **R.J.M. Konings:** Writing – review & editing, Supervision, Methodology. **A.L. Smith:** Writing – review & editing, Supervision, Project administration, Methodology, Funding acquisition, Formal analysis, Conceptualization.

Declaration of competing interest

The authors declare the following financial interests/personal relationships which may be considered as potential competing interests: Thomas Dumaire reports financial support was provided by Horizon 2020 European Innovation Council Fast Track to Innovation. Thomas

Data availability

Data will be made available on request.

Acknowledgments

Appendix A. Low temperature heat capacity of CrF$_2$

The existence of an antiferromagnetic transition in CrF$_2$ is confirmed by the low-temperature heat capacity data collected under varying magnetic fields (Fig. A.1). The anomaly shifts to slightly lower temperatures upon application of a magnetic field.

Fig. A.2 shows the measure low-temperature heat capacity together with the function at higher temperatures recommended in the IVTAN tables [41], showing the good accordance between the two temperature regimes.

Appendix B. Magnetization measurements of CrF$_2$

Magnetization measurements of CrF$_2$ show a clear anti-ferromagnetic order at T_N = 49.6 K, as reported by Stout et al. [52] and Boo et al. [49]. Measurements in DC and AC techniques confirmed this value (Figs. B.1).

Interestingly, below the anti-ferromagnetic transition temperature T_N, we observe a strong anisotropic behavior in the ordered state, that is of ferromagnetic type, similarly to anisotropic features reported below 308 K for antiferromagnetic Cr$_2$O$_3$ [53], or for some other
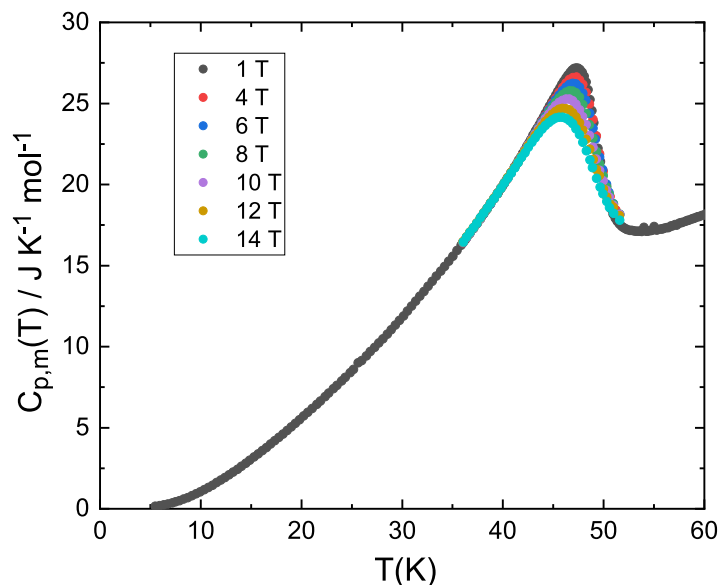
Fig. A.1. Evolution of the heat capacity of CrF_2 upon application of a magnetic field B = (1, 4, 6, 8, 10, 12, 14) Tesla.
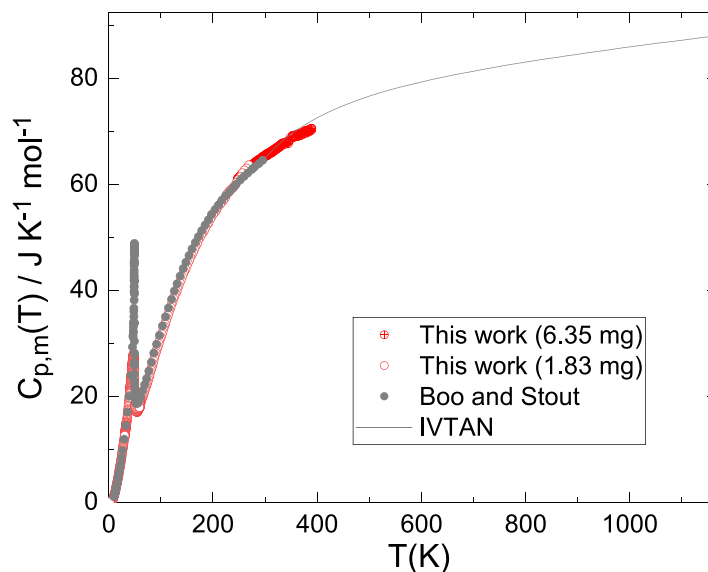

Fig. A.2. Evolution of the heat capacity of CrF_2 up to melting (1167 K).

reported Cr based materials [54]. Zero-Field Cooling (ZFC) measurements show negative response versus the applied magnetic field, while Field-Cooling (FC) curves at low magnetic fields are characteristics of a ferromagnetic-like ordered state. This ZFC diamagnetic response disappears at 10 kOe. The estimated coercitive field at 45 K is still 2500 Oe. ZFC and FC curves are joining at T_N, but difference between ZFC-FC magnetization curves is still present up to the maximum magnetic field applied (70 kOe). Neutron diffraction measurements [55] have shown CrF_2 to be a two-sublattice antiferromagnet with a distorted rutile structure of monoclinic symmetry, containing two Cr^{2+} ions per unit cell. This supports the intrinsic anisotropy features in the low temperature ordered state with a ferromagnetic canted moment responding strongly to applied magnetic fields. In the paramagnetic temperature range (T<T_N), we observe a very good reproducibility of DC magnetic susceptibility for all magnetic fields applied. Fitting

this paramagnetic field from 100 to 300 K by a modified Curie Weiss law, we obtain an effective moment μ_{eff} close to 5.7(3) μ_B, and a paramagnetic temperature θ_P close to −70 K. Cr^{2+} effective moment in the free ion model is 4.9 μ_B.

Appendix C. Ternary equilibria

In Fig. C.1, the isothermal sections calculated for different temperatures (750 K, 850 K, 950 K and 1050 K) in the ternary system $LiF - CrF_2 - ThF_4$, showing the stability of the solid phases.

Appendix D. Supplementary data

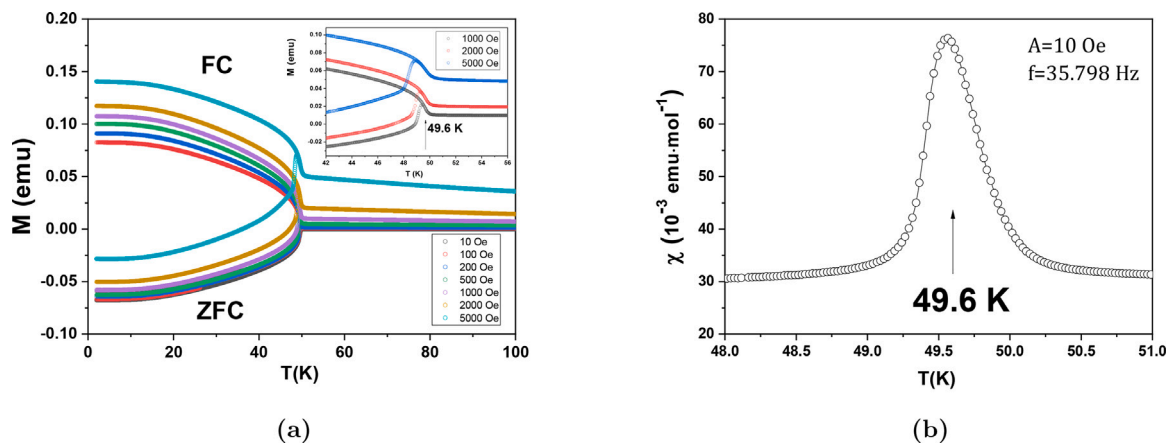Supplementary material related to this article can be found online at https://doi.org/10.1016/j.calphad.2024.102722.

Fig. B.1. (a) Evolution of the DC magnetization M of CrF$_2$ below T 100 K in ZFC and FC. (b) AC magnetic measurements showing the evolution of the AC magnetic susceptibility χ.
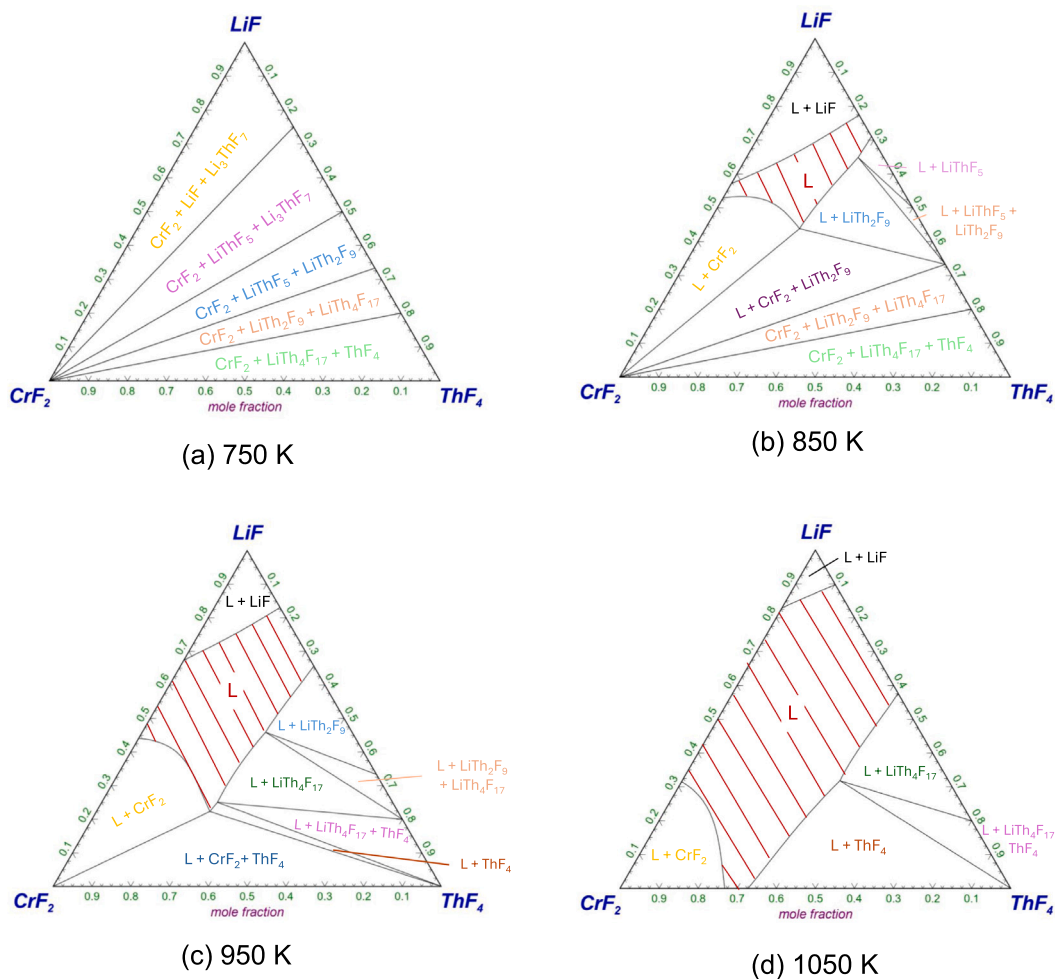

Fig. C.1. Isothermal sections of the ternary system LiF–CrF$_2$–ThF$_4$ at (a) 750 K, (b) 850 K, (c) 950 K and (d) 1050 K. The different stable solids and the liquid phases are indicated in the figures.

References

[1] J. Rogelj, D. Shindell, K. Jiang, S. Fifita, P. Forster, V. Ginzburg, C. Handa, H. Kheshgi, S. Kobayashi, E. Kriegler, L. Mundaca, R. Séférian, M.V. Vilariño, 2018: Mitigation pathways compatible with 1.5 °C in the context of sustainable development, in: V. Masson-Delmotte, P. Zhai, H.-O. Pörtner, D. Roberts, J. Skea, P. Shukla, A. Pirani, W. Moufouma-Okia, C. Péan, R. Pidcock, S. Connors, J.B.R. Matthews, Y. Chen, X. Zhou, M.I. Gomis, E. Lonnoy, T. Maycock, M. Tignor, T. Waterfield (Eds.), Global Warming of 1.5 °C. An IPCC Special Report on the Impacts of Global Warming of 1.5 °C above Pre-Industrial Levels and Related Global Greenhouse Gas Emission Pathways, in the Context of Strengthening the Global Response To the Threat of Climate Change, Sustainable Development, and Efforts To Eradicate Poverty, Intergovernmental Panel on Climate Change, 2018, pp. 93–174.

[2] D. LeBlanc, Molten salt reactors: A new beginning for an old idea, Nucl. Eng. Des. 240 (6) (2010) 1644–1656, http://dx.doi.org/10.1016/j.nucengdes.2009.12.033.

[3] J.E. Kelly, Generation IV International Forum: A decade of progress through international cooperation, Prog. Nucl. Energy 77 (2014) 240–246, http://dx.doi.org/10.1016/j.pnucene.2014.02.010.

[4] J. Serp, M. Allibert, O. Beneš, S. Delpech, O. Feynberg, V. Ghetta, D. Heuer, D. Holcomb, V. Ignatiev, J.L. Kloosterman, L. Luzzi, E. Merle-Lucotte, J. Uhlíř, R. Yoshioka, D. Zhimin, The molten salt reactor (MSR) in generation IV: Overview and perspectives, Prog. Nucl. Energy 77 (2014) 308–319, http://dx.doi.org/10.1016/j.pnucene.2014.02.014.

[5] O. Beneš, R.J.M. Konings, Molten salt reactor fuel and coolant, in: R.J.M. Konings, R.E. Stoller (Eds.), Comprehensive Nuclear Materials, Elsevier, Amsterdam, 2020, pp. 609–644, http://dx.doi.org/10.1016/b978-0-12-803581-8.11790-4.

[6] M. Allibert, M. Aufiero, M. Brovchenko, S. Delpech, V. Ghetta, D. Heuer, A. Laureau, E. Merle-Lucotte, 7 - Molten salt fast reactors, in: I.L. Pioro (Ed.), in: Woodhead Publishing Series in Energy, Woodhead Publishing, 2016, pp. 157–188, http://dx.doi.org/10.1016/B978-0-08-100149-3.00007-0, URL https://www.sciencedirect.com/science/article/pii/B9780081001493000070.

[7] O. Beneš, P. Souček, Molten salt reactor fuels, in: Advances in Nuclear Fuel Chemistry, Elsevier, Amsterdam, 2020, pp. 249–271, http://dx.doi.org/10.1016/b978-0-08-102571-0.00007-0.

[8] L. Mei, X. Cai, D. Jiang, J. Chen, W. Guo, W. Xiong, Investigation of thermal neutron scattering data for BeF_2 and LiF crystals, J. Nucl. Sci. Technol. 50 (4) (2013) 419–424, http://dx.doi.org/10.1080/00223131.2013.773169.

[9] M. Ubeyli, Neutronic performance of HYLIFE-II fusion reactor using various thorium molten salts, Ann. Nucl. Energy 33 (17–18) (2006) 1417–1423, http://dx.doi.org/10.1016/j.anucene.2006.09.006.

[10] D. Heuer, E. Merle-Lucotte, M. Allibert, M. Brovchenko, V. Ghetta, P. Rubiolo, Towards the thorium fuel cycle with molten salt fast reactors, Ann. Nucl. Energy 64 (2014) 421–429, http://dx.doi.org/10.1016/j.anucene.2013.08.002.

[11] Y. Liu, Y. Song, H. Ai, M. Shen, H. Liu, S. Zhao, Y. Liu, Z. Fei, X. Fu, J. Cheng, Corrosion of Cr in molten salts with different fluoroacidity in the presence of CrF_3, Corros. Sci. 169 (2020) 108636, http://dx.doi.org/10.1016/j.corsci.2020.108636.

[12] P.N. Haubenreich, J.R. Engel, Experience with the molten-salt reactor experiment, Nucl. Appl. Technol. 8 (2) (1970) 118–136, http://dx.doi.org/10.13182/nt8-2-118.

[13] J.W. Koger, Evaluation of Hastelloy N alloys after nine years exposure to both a molten fluoride salt and air at temperatures from 700 to 560 °C, 1972, http://dx.doi.org/10.2172/4468052, ORNL-TM-4189, URL https://www.osti.gov/biblio/4468052.

[14] W.D. Manly, J.H. Coobs, J.H. DeVan, D.A. Douglas, H. Inouye, P. Patriarca, T.K. Roche, J.L. Scott, Metallurgical problems in molten fluoride systems, IV, Prog. Nucl. Energy 2 (1960) 164–179.

[15] M. Kondo, T. Nagasaka, A. Sagara, N. Noda, T. Muroga, Q. Xu, M. Nagura, A. Suzuki, T. Terai, Metallurgical study on corrosion of austenitic steels in molten salt LiF–BeF2 (FLiBe), J. Nucl. Mater. 386–388 (2009) 685–688, http://dx.doi.org/10.1016/j.jnucmat.2008.12.317.

[16] K. Sridharan, T.R. Allen, Corrosion in molten salts, in: Molten Salts Chemistry, Elsevier, Amsterdam, 2013, pp. 241–267, http://dx.doi.org/10.1016/b978-0-12-398538-5.00012-3.

[17] M. Liu, J. Zheng, Y. Lu, Z. Li, Y. Zou, X. Yu, X. Zhou, Investigation on corrosion behavior of Ni-based alloys in molten fluoride salt using synchrotron radiation techniques, J. Nucl. Mater. 440 (1) (2013) 124–128, http://dx.doi.org/10.1016/j.jnucmat.2013.04.056, URL https://www.sciencedirect.com/science/article/pii/S0022311513006740.

[18] G. Zheng, K. Sridharan, Corrosion of structural alloys in high-temperature molten fluoride salts for applications in molten salt reactors, J. Minerals Metals Mater. Soc. 70 (8) (2018) 1535–1541, http://dx.doi.org/10.1007/s11837-018-2981-2.

[19] H. Sun, X. Ding, H. Ai, G. Lei, X. Yang, J.-Q. Wang, Interaction mechanisms of a Hastelloy N-316L stainless steel couple in molten LiF-NaF-KF salt, Corros. Sci. 164 (2020) 108317, http://dx.doi.org/10.1016/j.corsci.2019.108317.

[20] Q. Jie, Z. Yang, Y. Guo-Jun, H. Shang-Ming, L. Wen-Guan, J. Yan-Yan, L. Zhi-Jun, X. Hong-Jie, Speciation study of chromium corrosion product in molten LiF-NaF-KF salt, Nucl. Sci. Tech. 26 (2015) 127–130, http://dx.doi.org/10.13538/j.1001-8042/nst.26.060602.

[21] T. Dumaire, R.J.M. Konings, A.L. Smith, Thermodynamic assessment of the AF–CrF3 (A=Li, Na, K) and CrF2–CrF3 systems, Thermo 1 (2021) 205–219, http://dx.doi.org/10.3390/thermo1020014.

[22] P. Souček, O. Beneš, B. Claux, E. Capelli, M. Ougier, V. Tyrpekl, J.-F. Vigier, R.J. Konings, Synthesis of UF4 and ThF4 by HF gas fluorination and re-determination of the UF4 melting point, J. Fluor. Chem. 200 (2017) 33–40, http://dx.doi.org/10.1016/j.jfluchem.2017.05.011.

[23] E. Capelli, O. Beneš, M. Beilmann, R.J.M. Konings, Thermodynamic investigation of the LiF–ThF4 system, J. Chem. Thermodyn. 58 (2013) 110–116, http://dx.doi.org/10.1016/j.jct.2012.10.013, URL https://www.sciencedirect.com/science/article/pii/S0021961412003990.

[24] C. Poulenc, Contribution à l'étude des fluorures anhydres et cristallisés, in: Berthelot, Pasteur, Friedel, Mascart (Eds.), Annales de Chimie et de Physique, No. 2 in 7, G. Masson, Paris, 1894, pp. 5–77.

[25] A. de Kozak, Comptes rendus hebdomadaires des séances de l'Académie des sciences, (268) Académie des sciences de Paris, Paris, 1969, pp. 416–418, Série C.

[26] A. de Kozak, Etude de quelques composes fluores du chrome, Rev. Chim. Miner. 8 (1971) 301–337.

[27] O. Levy, B. Bogoslavsky, A. Bino, Anhydrous chromous acetate revisited – a very simple synthetic route, Inorg. Chim. Acta 391 (2012) 179–181, http://dx.doi.org/10.1016/j.ica.2012.04.029.

[28] L.B. McCusker, R.B.V. Dreele, D.E. Cox, D. Louër, P. Scardi, Rietveld refinement guidelines, J. Appl. Crystallogr. 32 (1) (1999) 36–50, http://dx.doi.org/10.1107/s0021889898009856.

[29] J. Rodriguez-Carvajal, Recent advances in magnetic structure determination by neutron powder diffraction, Physica B 192 (1–2) (1993) 55–69.

[30] W.J. Boettinger, U.R. Kattner, K.-W. Moon, J.H. Perepezko, NIST recommended practice guide: DTA and Heat-flux DSC Measurements of Alloy Melting and Freezing, in: National Institute of Standards and Technology (Ed.), U.S. Government Printing Office, Washington, DC, 2006, http://dx.doi.org/10.6028/nbs.sp.960-15.

[31] O. Beneš, R.J. Konings, S. Wurzer, M. Sierig, A. Dockendorf, A DSC study of the NaNO3–KNO3 system using an innovative encapsulation technique, Thermochim. Acta 509 (1–2) (2010) 62–66, http://dx.doi.org/10.1016/j.tca.2010.06.003.

[32] J. Lashley, M. Hundley, A. Migliori, J. Sarrao, P. Pagliuso, T. Darling, M. Jaime, J. Cooley, W. Hults, L. Morales, D. Thoma, J. Smith, J. Boerio-Goates, B. Woodfield, G. Stewart, R. Fisher, N. Phillips, Critical examination of heat capacity measurements made on a quantum design physical property measurement system, Cryogenics 43 (6) (2003) 369–378, http://dx.doi.org/10.1016/s0011-2275(03)00092-4.

[33] C.W. Bale, P. Chartrand, S. Degterov, G. Eriksson, K. Hack, R.B. Mahfoud, J. Melançon, A. Pelton, S. Petersen, FactSage thermochemical software and databases, CALPHAD 26 (2) (2002) 189–228.

[34] U.R. Kattner, H.J. Seifert, H.L. Lukas, Editorial: Integrated computational materials engineering, CALPHAD, CALPHAD, Comput. Coupling Phase Diagr. Thermochem. 34 (2010) 385–386, http://dx.doi.org/10.1016/j.calphad.2010.10.005.

[35] Y.A. Chang, S. Chen, F. Zhang, X. Yan, F. Xie, R. Schmid-Fetzer, W.A. Oates, Phase diagram calculation: past, present and future, Prog. Mater. Sci. 49 (3–4) (2004) 313–345, http://dx.doi.org/10.1016/s0079-6425(03)00025-2.

[36] J.A. Ocádiz Flores, R.J.M. Konings, A.L. Smith, Using the Quasi-chemical formalism beyond the phase Diagram: Density and viscosity models for molten salt fuel systems, J. Nucl. Mater. 561 (2022) 153536, http://dx.doi.org/10.1016/j.jnucmat.2022.153536.

[37] R. Thoma, H. Insley, B. Landau, H. Friedman, W. Grimes, Phase equilibria in the fused salt systems LiF–ThF4 and NaF–ThF4, J. Phys. Chem. 63 (8) (1959) 1266–1274.

[38] E. Capelli, O. Beneš, R.J.M. Konings, Thermodynamic assessment of the LiF–ThF4–PuF3–UF4 system, J. Nucl. Mater. 462 (2015) 43–53, http://dx.doi.org/10.1016/j.jnucmat.2015.03.042.

[39] Joint Research Centre - European Commission, Joint Research Centre Molten Salt Database - JRCMSD, https://joint-research-centre.ec.europa.eu/joint-research-centre-molten-salt-database-jrcmsd_en, Accessed: 2024-02-05.

[40] A. Tosolin, E. Capelli, R. Konings, L. Luzzi, O. Beneš, Isobaric heat capacity of solid and liquid thorium tetrafluoride, J. Chem. Eng. Data 64 (9) (2019) 3945–3950, http://dx.doi.org/10.1021/acs.jced.9b00348.

[41] V.S. Iorish, N.M. Aristova, G. Bergman, L. Gorohov, A. Gusarov, Y. Yezhov, A. Kulikov, E. Osina, E. Shenyavskaya, N. Handamirova, V. Jungmann, Thermodynamic Properties of Substances (1978–2004), Publishing House Nauka, Moscow, Russia, 2004.

[42] J. Malcolm W. Chase, National Information Standards Organization (US), NIST-JANAF Thermochemical Tables, fourth ed., American Intitute of Physics, New York, 1998.

[43] J.P.M. van der Meer, R.J.M. Konings, Thermal and physical properties of molten fluorides for nuclear applications, J. Nucl. Mater. 360 (1) (2007) 16–24, http://dx.doi.org/10.1016/j.jnucmat.2006.08.010.

[44] E. Capelli, R.J.M. Konings, Halides of the actinides and fission products relevant for molten salt reactors, in: R.J. Konings, E. Stoller Roger (Eds.), Comprehensive Nuclear Materials, Second ed., vol. 7, Elsevier, Amsterdam, 2020, pp. 256–283, http://dx.doi.org/10.1016/b978-0-12-803581-8.11794-1.

[45] A.D. Pelton, S. Degterov, G. Eriksson, C. Robelin, Y. Dessureault, The modified quasichemical model I—binary solutions, Metall. Mater. Trans. B 31 (4) (2000) 651–659, http://dx.doi.org/10.1007/s11663-000-0103-2.

[46] O. Beneš, M. Beilmann, R.J.M. Konings, Thermodynamic assessment of the LiF–NaF–ThF$_4$–UF$_4$ system, J. Nucl. Mater. 405 (2) (2010) 186–198, http://dx.doi.org/10.1016/j.jnucmat.2010.08.017.

[47] A.D. Pelton, A general ''geometric'' thermodynamic model for multicomponent solutions, CALPHAD 25 (2) (2001) 319–328, http://dx.doi.org/10.1016/s0364-5916(01)00052-9.

[48] B.J. Sturm, Phase equilibria in the system chromium (II) fluoride-chromium (III) fluoride, Inorg. Chem. 1 (3) (1962) 665–672.

[49] W.O.J. Boo, J.W. Stout, Heat capacity and entropy of CuF$_2$ and CrF$_2$ from 10 to 300 K. Anomalies associated with magnetic ordering and evaluation of magnetic contributions to the heat capacity, J. Chem. Phys. 71 (1) (1979) 9–16, http://dx.doi.org/10.1063/1.438064.

[50] P.E. Lim, J.W. Stout, Polarized crystal spectra of CrF$_2$ from 6000 to 38000 cm^{-1}, The Journal of Chemical Physics 63 (11) (1975) 4886–4902, http://dx.doi.org/10.1063/1.431232.

[51] P.E. Lim, J.W. Stout, Erratum:, J. Chem. Phys. 68 (9) (1978) 4331, http://dx.doi.org/10.1063/1.436336.

[52] J.W. Stout, P. DeLassur, C.D. Graham, J.J. Rhyne, Crf$_2$, a canted antiferromagnet, in: AIP Conference Proceedings, AIP, 1972, http://dx.doi.org/10.1063/1.3699510.

[53] H. Wiegelmann, A.G.M. Jansen, P. Wyder, J.-P. Rivera, H. Schmid, Magnetoelectric effect of Cr$_2$O$_3$ in strong static magnetic fields, Ferroelectrics 162 (1) (1994) 141–146, http://dx.doi.org/10.1080/00150199408245099.

[54] A.N. Vasiliev, O.S. Volkova, E. Hammer, R. Glaum, J.-M. Broto, M. Millot, G. Nénert, Y.T. Liu, J.-Y. Lin, R. Klingeler, M. Abdel-Hafiez, Y. Krupskaya, A.U.B. Wolter, B. Büchner, Weak ferrimagnetism and multiple magnetization reversal α-Cr$_3$(PO$_4$)$_2$, 85 (1) (2012) 014415, http://dx.doi.org/10.1103/physrevb.85.014415.

[55] J.W. Cable, M.K. Wilkinson, E.O. Wollan, Neutron diffraction studies of antiferromagnetism in CrF$_2$ and CrCl$_2$, Phys. Rev. 118 (1960) 950.